Journal of Energy Storage 169 (2026) 122723

Contents lists available at ScienceDirect

Journal of Energy Storage

journal homepage: www.elsevier.com/locate/est

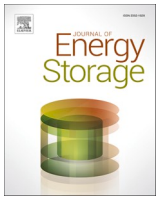

Research Papers

U-tube macro-encapsulation of phase change material for efficient utilization of latent energy storage in solar desalination system: A comprehensive experimental study

Vikash Kumar Chauhan [a,*], Pushkar Singh [b], Rohit Kumar Singh [a], Suresh Pratap [a], Vineet Singh [c], Shailendra Kumar Shukla [d]

[a] Department of Mechanical Engineering, G.L. Bajaj Institute of Technology and Management, Greater Noida, 201306, India
[b] Department of Mechanical Engineering, National Institute of Technology, Uttarakhand Srinagar, Pauri (Garhwal), 246174, India
[c] Department of Mechanical Engineering, School of Engineering & Technology, IFTM University, Moradabad, 244102, India
[d] Centre for Energy and Resources Development, Department of Mechanical Engineering, Indian Institute of Technology (BHU), Varanasi, 221005, India

ARTICLE INFO

Keywords:
Solar desalination
Heat storage efficiency
Hemispherical solar still
U-tube encapsulation
Economic study
Environmental impact

ABSTRACT

Freshwater scarcity is a global challenge, and this study presents a sustainable solution using solar energy and thermal storage. In the present work, the performance of a conventional solar still (CSS) enriched with lauric acid as phase change material (PCM) is compared with a hemispherical solar still (HSSS) with a novel encapsulation configuration. It studies how the position and encapsulation of PCM affect the performance. To investigate this, three configurations, namely CSS integrated with PCM beneath the absorber surface (CSS-PCM), a hemispherical solar still with PCM beneath the absorber surface (HSSS-PCM), and a hemispherical solar still with U-tube macro-encapsulated PCM above the absorber surface (HSSS-PCM-ME), were fabricated and tested. It was found that PCM beneath the absorber surface resulted in peak PCM temperatures of 51 °C and 53 °C above the melting point. However, it allowed for a partial phase change, with a phase change time of less than 2 h and total energy stored of 3048 kJ and 3138 kJ, yielding storage efficiencies of 31.9% and 51.5%, respectively. On the other hand, the U-tube macro-encapsulation design enabled direct charging, leading to higher maximum PCM temperature of 56 °C, with longer phase-change duration of 5 h, and a higher total energy stored of 3273 kJ, with a higher storage efficiency of 79.5%. A sensitivity analysis of ±10% variation in the released-energy fraction resulted in absolute deviations of ±3.2% to ±7.9%, indicating consistent system behavior. At the system level, the daily cumulative freshwater yield increases from 2350 mL/m^2 with CSS-PCM to 2580 mL/m^2 with HSSS-PCM and 3240 mL/m^2 with HSSS-PCM-ME. The maximum overnight yield was 1030 mL/m^2 with macro-encapsulated PCM. Similarly, the thermal efficiencies of the systems were 34.61%, 38.74%, and 44.22%, respectively, while the maximum exergy efficiency was 3.4% with HSSS-PCM-ME. Additionally, the techno-economic-environmental evaluation indicates that the payback period of the macro-encapsulated system is 10.3 months, and its CO_2 reduction potential is 565.65 kg/year.

Nomenclature

Symbol	Description	Unit
T_w	Basin water temperature	°C
T_g	Condenser (glass) temperature	°C
T_{pcm}	Phase change material temperature	°C
T_a	Ambient temperature	°C
η_{th}	Thermal efficiency	%
η_{ex}	Exergy efficiency	%
L_v	Latent heat of vaporization of water	kJ/kg
L_f	Latent heat of fusion of PCM	kJ/kg
I_s	Solar irradiation	W/m^2
A_s	Absorber surface area	m^2
$\dot{m}$	Distillate yield rate	kg/h
E_{solar}	Utilized solar energy	kWh/year

(continued on next column)

(continued)

(continued on next page)

* Corresponding author at: Department of Mechanical Engineering, G.L. Bajaj Institute of Technology and Management, Plot No. 2, APJ Abdul Kalam Road, Knowledge Park-III, Greater Noida, Uttar Pradesh, 201306, India.
E-mail address: er.vikashchauhan@gmail.com (V.K. Chauhan).

https://doi.org/10.1016/j.est.2026.122723
Received 13 January 2026; Received in revised form 23 April 2026; Accepted 17 May 2026
Available online 19 May 2026

(*continued*)

E_{fgrid}	Grid emission factor	kg CO_2/kWh
T_{sun}	Sun temperature	K
f	Fraction of thermal energy released	–

Abbreviation	Description
CSS	Conventional Single Slope Solar Still
CSS-PCM	Conventional Single Slope Solar Still with PCM
HSSS	Hemispherical solar still
HSSS-PCM	Hemispherical solar still with PCM
HSSS-PCM-ME	Hemispherical solar still with macro-encapsulated PCM
PCM	Phase change material
FRP	Fiber reinforced polymer
DSC	Differential scanning calorimetry
TGA	Thermogravimetric analysis
TDS	Total dissolved solids
EC	Electrical conductivity
TFC	Total fabrication cost
AFC	Annual first cost
AMC	Annual maintenance cost
PP	Payback period
AAP	Average annual production
OAG	Overall annual gain
IPCC	Intergovernmental Panel on Climate Change
CEA	Central Electricity Authority
LTES	Latent thermal energy storage
LHS	Latent heat stored
SHS	Sensible heat stored
THS	Total heat stored
UHR	Useful heat released

1. Introduction

There is an urgent need to develop sustainable methods for producing freshwater amid disturbances to the hydrological cycle, groundwater depletion, and rising population demand [1,2]. Water stress levels have increased by 2.8% globally since 2015, reaching 18.6% in 2021 [3]. Although seas and oceans contain about 97% of the world's accessible water, they are saline. Desalination technology based on solar energy has proven to be a more economical and sustainable approach to addressing water scarcity [4]. The oldest known method of purifying water is solar desalination, which provides a useful alternative for communities worldwide, particularly in isolated areas with ample sunshine [5–7]. Through thermal evaporation and condensation, solar stills (SS) provide a sustainable, environmentally friendly method for converting saline water into freshwater. However, low yields and efficiency limit the use of solar-powered desalination systems, which now account for less than 0.65% of all desalination plant capacity [8].

One way to improve performance of SS is to store the excess solar energy into heat storage materials. To prolong the functioning of SSs, various phase change material (PCM) like organic (paraffin), fatty acids (palmitic acid stearic acid), and salt hydrates have been investigated. With single slope SS known as conventional SS [9,10] as base line, modified versions of SS like double slope SS [11], tubular SS [12,13], pyramid SS [14,15], prism SS, inverted SS, multi basin SS, wick type [16], triangular SS [17], inclined SS like wick type and stepped SS [18], and hemispherical SS have been investigated in conjugation with PCM. A single-slope solar still incorporated with PCM exhibited a maximum thermal efficiency of 27.7% [19]. Weir-type cascaded SS integrated with paraffin wax, reported a thermal efficiency of 31%, primarily limited by poor heat transfer between the PCM and basin water [20].

Experimental investigations show that PCM placed beneath the absorber surface often results in higher thermal resistance than when placed above the absorber surface in basin water [21,22]. While placed below the absorber surface, it restricts effective latent heat transfer and reduces overall storage capacity, also leading to a bulky configuration [23,24]. Thereafter, encapsulation geometries come into play, allowing convenient heat transfer between the PCM and the basin water [25–27]. Various types of geometries have been investigated to encapsulate the PCM and integrate with different designs of SS, like spherical, tubular, cylindrical and rectangular [28]. Approximately 60% of PCM encapsulation studies in solar stills have been conducted on conventional single-slope designs, while hemispherical solar stills remain the least studied geometry. Among these encapsulation studies, approximately 70% employed macroencapsulation techniques, with or without extended surfaces, highlighting their prevalence for PCM integration [29]. A CSS integrated with a steel tube encapsulated in paraffin wax, submerged in basin water, has been investigated and compared with performance with and without PCM integration, showing an average thermal efficiency improvement of 19.9% [30]. A comparative study was performed on CSS and pyramidal SS, using lauric acid in three different forms: placed below the absorber surface, encapsulated in cans, and in copper tubes. Results show that freshwater yield was 2.03 L/m^2 with CSS and increased by 22.3%, 57.7%, and 51.23% with the below basin, cans, and copper tube configurations, respectively. Superior performance with copper tubes was also supported by heat transfer of 26.55 W/m^2K and the highest thermal efficiency of 36.5% [31].

A popular design of HSSS, provides a larger condensation area without shadowing effect was used with PCM (beneath the absorber surface) were experimentally investigated and achieved 46% thermal efficiency and 3.88% exergy efficiency. In contrast, in another experiment with the same PCM, the model achieved 45% thermal efficiency due to changes in configuration and placement of PCM [32,33]. It is found that hemispherical SS integrated with PCM reports decent efficiency but suffers from incomplete phase transition and a bulky geometry when placed below the absorber surface [34]. HSSS was numerically investigated with paraffin wax placed beneath the basin absorber surface, achieving a thermal efficiency of 31% at 5 kg of PCM. In another study, HSSS and paraffin wax achieved a thermal efficiency 41.43% [35]. With the encapsulation strategy, HSSS with aluminum cans filled with paraffin wax was investigated in triangular (3 cans) and rectangular (4 cans) configurations. As a result, thermal efficiency improved by 67.2% and 92.9% due to efficient heat transfer and utilization [36]. However, with this encapsulation, it was not possible to capture solar irradiation effectively due to the cans' limited surface area. Hence, from the above investigations, it is concluded that HSSS with high exposure-area encapsulation geometry has not been investigated thoroughly.

The present experimental investigation presents a comprehensive analysis of a hemispherical solar still with a novel high-exposure-area PCM encapsulation configuration. U-tube macro-encapsulation of PCM (lauric acid) with a novel absorber surface, enabling a high rate of charging and improved PCM-water heat exchange. Under real climatic conditions, this investigation compares the performance of conventional and modified hemispherical solar stills. With a novel configuration, storage efficiency reached 79.5%, with a freshwater yield of 3240 mL/m^2 and a thermal efficiency of 44.22%, surpassing the other two models. Moreover, it aims to quantify the combined improvements in energy, exergy, economic, and environmental (4E) performance of desalination systems. It further seeks to develop a scalable and thermodynamically efficient desalination configuration that operates using sustainable and cost-effective clean energy sources.

2. Methods and materials

2.1. Solar stills with PCM test rigs

Three solar still configurations, namely a conventional single-slope solar still with PCM (CSS-PCM) having tilt angle of 25° (latitude of experimental location), a hemispherical slope solar still with PCM (HSSS-PCM) and a hemispherical slope solar still with PCM-encapsulation (HSSS-PCM-ME), were fabricated and installed side by side to ensure identical boundary conditions as shown in Fig. 1. The basin body was made from a fiber-reinforced plastic (FRP) sheet of 3 mm thickness to ensure minimal heat loss from the base and side walls, with structural integrity and corrosion resistance. Each SSs had an effective

Fig. 1. Experimental setup of solar stills integrated with PCM namely Conventional single slope solar still (CSS-PCM), Hemispherical Solar still (HSSS-PCM), Hemispherical Solar still (HSSS-PCM-ME).

basin absorber area of 1 m^2. Polymethyl methacrylate (PMMA) was used as the condenser surface of 3 mm thickness due to its ability to mold in required curvature and its mechanical stability compared to glass. Synthetic saline water was fed into the SSs, with a total dissolved solids (TDS) concentration of 35,000 ppm to simulate seawater conditions. Further, lauric acid as a PCM was used to store daytime excess energy as latent heat energy. Here, PCM is placed beneath the absorber surface in CSS-PCM and HSSS-PCM. In HSSS-PCM-ME, PCM was placed above the absorber surface in a novel encapsulation design. All the measurements were recorded at 1 h intervals from 09:00 h to 22:00 h on several experimental days.

2.2. U-tube macro-encapsulation of PCM

Fig. 2 shows the schematic diagram of working setups and encapsulation configuration where Fig. 2(a) shows CSS model with PCM beneath absorber surface, Fig. 2(b) shows HSSS model with PCM beneath absorber surface and Fig. 2(c) shows HSSS model with encapsulated PCM attached with advanced absorber surface of copper above FRP absorber surface. The PCM was placed in a U-tube encapsulated layout made of copper tubes having wall thickness of 2 mm and internal diameter of 36 mm. During the charging phase under sunlight, solar energy absorbed by the black-coated copper plate (pseudo absorber surface) as shown in Fig. 2(d) and distributed within PCM by conduction, resulting in sensible and latent heat storage. During the discharging phase, the molten PCM releases stored heat energy, which is conducted from the plate and tubes and gets redistributed within the basin water by buoyancy-driven convection.

2.3. Characterization of PCM

Lauric acid (dodecanoic acid) of commercial reagent grade (purity ≥98%), supplied by Sigma-Aldrich (India), was used as the PCM. A constant mass of 15 kg was filled in all three configurations. The material was used as-received without further purification, and its thermophysical properties were verified through DSC and TGA characterization (Section 3.1) before deployment. Differential scanning calorimetry (DSC) was carried out using a Shimadzu DSC-60 Plus (temperature accuracy ±0.1 °C; heat-flow sensitivity 0.2 μW) to determine the phase-change temperature and latent heat of lauric acid, which govern its energy storage performance. Measurements were performed at 5 °C/min over 25–75 °C under nitrogen atmosphere. Thermogravimetric analysis (TGA) was conducted using a Shimadzu TGA − 50 (balance sensitivity 0.1 μg) from ambient to 350 °C at 10 °C/min to assess thermal stability and decomposition behavior under elevated temperatures.

2.4. Thermal efficiency of solar still

Thermal efficiency (η) represents the ratio of useful output energy to total input energy, consistent with the first law of thermodynamics applied to an open evaporative system. In a solar still, the useful energy output is not simply heat but the latent heat of vaporization, i.e., the energy required to convert liquid water into vapor. This is captured by the evaporative mass flux directly reflects the system's productive output. The denominator represents the total solar energy incident on the absorber surface, which is the primary energy source driving the thermodynamic cycle of evaporation-condensation. Any modification that leads to more effective use of heat in the system such as improved heat storage, lower heat resistance, or extended evaporation time will automatically lead to an increase in the value of the numerator, which means that efficiency is increased using Eq. (1) [37,38].

$$\eta_{th} = \frac{\Sigma \dot{m}_e L_v}{I(t)s \times A_s \times 3600} \tag{1}$$

Here, η_{th} is thermal efficiency, $\dot{m}_e$ is freshwater yield (kg/h), L_v is latent heat of vaporization of water (kJ/kg) at basin water temperature, $I(t)_s$ is the solar irradiation (W/m^2), and A_s is absorber surface area (1 m^2).

2.5. Exergy efficiency of solar stills

Exergy efficiency in solar stills is an approach to measuring their performance from a second-law perspective, considering not only the amount of energy used but also its quality and the losses due to irreversibilities. The difference between thermal efficiency, which represents the conversion of solar energy to latent energy, and exergy efficiency is that the latter measures the usefulness of the energy used. It can be estimated as the ratio of total exergy output ($Ex_{,out}$) to total exergy input (Ex_{in}) with respect to freshwater production using Eqs. (2)–(4), [38,39].

$$\eta_{Ex} = \frac{Ex_{out}}{Ex_{in}} \tag{2}$$

$$Ex_{out} = \frac{\dot{m}_e L_v}{3600}\left(1 - \frac{T_a}{T_w}\right) \tag{3}$$

$$Ex_{in} = I(t)_s A_b \left(1 - \frac{4T_a}{3T_s} + \frac{1}{3}\left(\frac{T_a}{T_s}\right)^4\right) \tag{4}$$

Here, T_a is ambient temperature (K), T_w is basin or saline water temperature (K), T_s is the sun's surface temperature taken as 6000 K [39].

The term $Ex_{,out}$ represents the useful exergy of evaporated water, corrected by the Carnot factor $\left(1\frac{T_a}{T_w}\right)$, which accounts for the finite temperature difference between the basin water and ambient conditions. This indicates that only a fraction of the latent heat contributes to useful work potential, while the rest is thermodynamically degraded. The input exergy $Ex_{,in}$ incorporates the Petela factor [39], which estimates the maximum work potential of solar radiation, indicating that while solar energy is high-grade, its conversion into low-temperature heat in a solar still leads to significant thermodynamic degradation.

2.6. Data acquisition and uncertainty analysis

2.6.1. Data acquisition

All measurements were performed using calibrated instruments. K-type thermocouples were used to record basin water temperature (two locations), PCM temperature (at four locations), and condenser surface

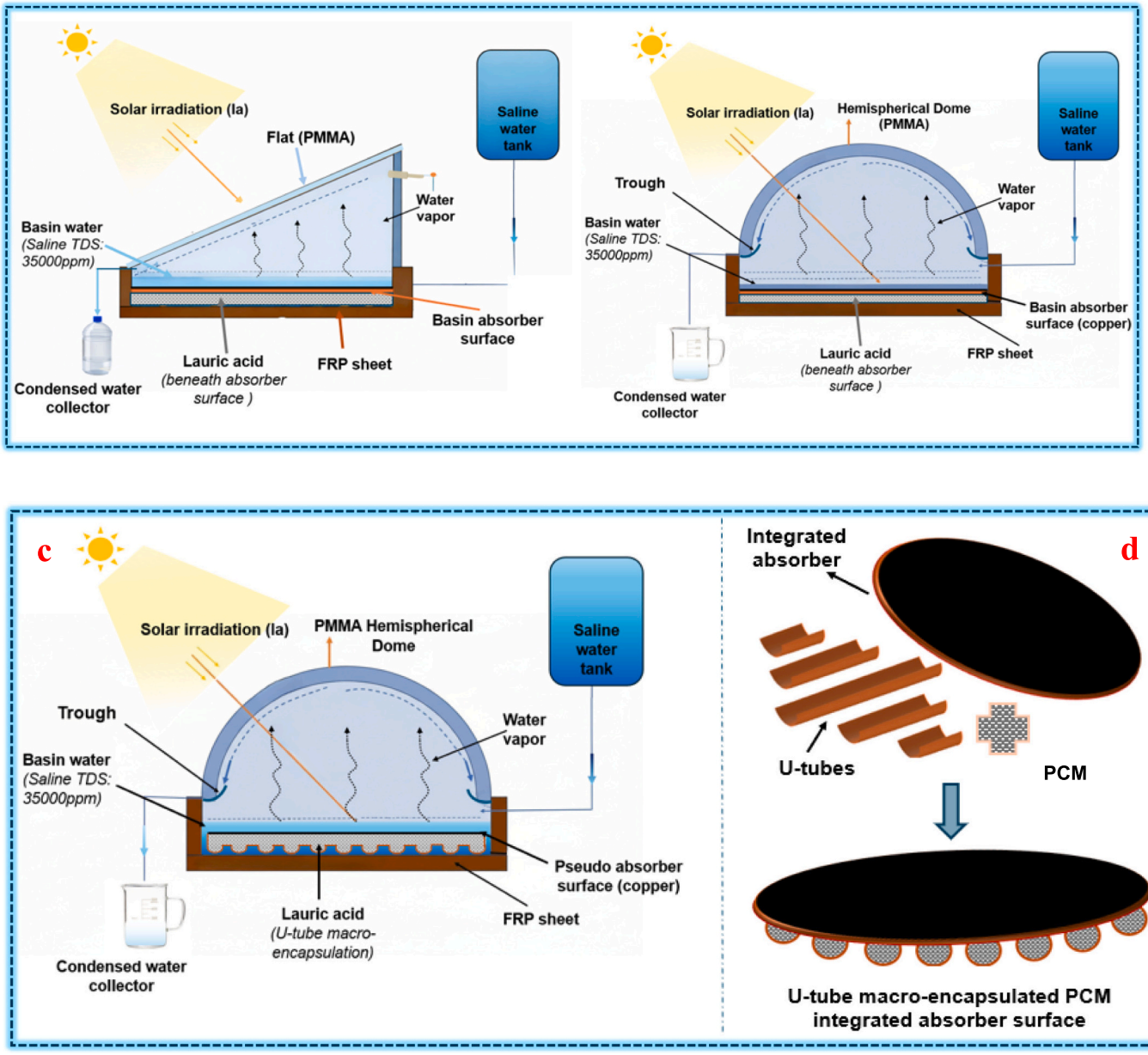

Fig. 2. Schematic design of solar stills. (a) Conventional Single Slope Solar Still PCM-below (CSS-PCM) (b) Hemispherical Solar Still PCM-below (HSS-PCM) (c) Hemispherical Solar Still macro-encapsulated PCM (HSS-PCM-ME), and (d) U-tube encapsulation configuration with attached copper absorber surface.

temperature (inner and outer surface). Additionally, ambient temperature and solar irradiance was measured by a thermometer and pyranometer recorded at 60-min intervals using a data logger. Freshwater yield was measured using a graduated collector. A float-type water-level sensor (HC-SR04 ultrasonic module, resolution ±1 mm) was interfaced with an Arduino Uno microcontroller, which activated a solenoid valve connected to an external saline-water reservoir whenever the basin water depth fell below 25 mm. This IoT-based feedback loop maintained a constant basin water depth of 25 ± 1 mm throughout the experimental period, eliminating the need for manual intervention and ensuring reproducible thermal boundary conditions across all three solar still configurations.

2.6.2. *Uncertainty analysis*

In the present experimental work, data were collected and recorded using various instruments. To ensure the reliability of those instruments, an uncertainty analysis was performed. Table 1 outlines the accuracy, range, resolution, and external uncertainty (standard uncertainty) of each measuring instrument like the pyranometer, thermometer, K-type thermocouple, and measuring flask. Standard uncertainties are determined using Eqs. (5)–(6). Further error analysis of the calculated variables was performed using the error propagation method, as shown in

Table 1
Summary of uncertainty analysis of instruments with accuracy, range and resolution for reliable measurement.

S. N.	Instruments	Accuracy	Range	Resolution	Uncertainty value
1	K-type thermocouple	±1 °C	−100 °C to 1300 °C	1 °C	0.5 °C
2	Pyranometer	±10 W/m^2	0–1999 W/m^2	1 W/m^2	4 W/m^2
3	Measuring flask	±5 mL	0–1000 mL	10 mL	3 mL
4	Ambient thermometer	±1 °C	−50 °C–70 °C	0.5 °C	0.5 °C

Eqs. (7)–(9) [40].

$$U_{E,x} = \left(\frac{a_x^2}{3}\right)^{0.5} \tag{5}$$

$$U = \left(\sum_i U_i^2\right)^{0.5} \tag{6}$$

Error propagation in derived quantities is estimated by Eq. (7),

$$U_X = \sqrt{\left(\frac{\partial X}{\partial x_1}U_1\right)^2 + \left(\frac{\partial X}{\partial x_2}U_2\right)^2 + \cdots + \left(\frac{\partial X}{\partial x_n}U_n\right)^2} \tag{7}$$

Error propagation in thermal efficiency estimation is calculated by Eq. (8),

$$U_{\eta_{th}} = \sqrt{\left(\frac{\partial \eta_{th}}{\partial m}U_m\right)^2 + \left(\frac{\partial \eta_{th}}{\partial I(t)}U_{I(t)}\right)^2} \tag{8}$$

Error propagation in exergy efficiency estimation is calculated by Eq. (9),

$$U_{\eta_{ex}} = \sqrt{\left(\frac{\partial \eta_{ex}}{\partial m}U_m\right)^2 + \left(\frac{\partial \eta_{ex}}{\partial I(t)}U_{I(t)}\right)^2 + \left(\frac{\partial \eta_{ex}}{\partial T_w}U_{T_w}\right)^2 + \left(\frac{\partial \eta_{ex}}{\partial T_a}U_{T_a}\right)^2} \tag{9}$$

In this equation, U_X is the uncertainty of the derived parameters like $U_{\eta_{th}}$ and $U_{\eta_{ex}}$, while U_1, U_2 are the standard uncertainty of measuring instruments like U(I(t)), U(T_w), and U(T_a) refer to the uncertainties of distillate solar radiation irradiation, the water temperature in the basin, and the ambient air temperature measurements, respectively.

2.7. Energy-economic and environment

The energy–economic assessment is crucial for determining the real-world viability of solar still systems by linking technical performance with financial returns. It evaluates fabrication cost, annualized cost, water production, and payback period to assess affordability and scalability. The analysis assumes a system lifetime of 5 years, an interest rate of 8%, a constant distilled water price of ₹20/L, money recovery factor (MRF) of 0.277 and uses standard cost relations such as CRF, AFC, and AMC for economic estimation [41,42].

Capital Recovery Factor (CRF),

$$\mathrm{CRF} = \frac{\mathrm{i}\,(1+\mathrm{i})^{\mathrm{n}}}{(1+\mathrm{i})^{\mathrm{n}} - 1} \tag{10}$$

where I is interest rate and n are system lifetime (years, taken as 5 years).

Annual first cost (AFC):

$$\mathrm{AFC} = \mathrm{TFC} \times \mathrm{CRF} \tag{11}$$

Annual maintenance cost (AMC):

$$\mathrm{AMC} = 0.20 \times \mathrm{AFC} \tag{12}$$

Payback period (PP):

$$\mathrm{PP} = \frac{\mathrm{TFC}}{(\mathrm{OAG} - \mathrm{AMC})} \tag{13}$$

The environmental assessment focuses on quantifying sustainability through CO_2 emission mitigation achieved by utilizing solar energy instead of grid electricity. It estimates avoided emissions using national (CEA) and global (IPCC) emission factors, assuming constant grid emission intensity and annual solar energy utilization. This approach highlights the potential of solar stills in reducing carbon footprint while supporting clean water production.

CO_2 emissions avoided:

$$\mathrm{CO_2avoided} = \mathrm{Esolar} \times \mathrm{Ef,grid} \tag{14}$$

where E_{solar} is the annual solar energy utilized (kWh/year) and $E_{f,grid}$ is the grid emission factor (kg CO_2/kWh). For the Indian grid: $E_{f,grid}$ is 0.926 kg CO_2/kWh (CEA India [43]), and for global average $E_{f,grid}$ is 0.34 kg CO_2/kWh (IPCC [44]).

3. Results and discussion

3.1. Characterization of lauric acid

As a PCM, lauric acid was used to store the latent and sensible heat. Fig. 3(a) shows the DSC analysis of lauric acid, which was performed from 20 to 75 °C at a heating rate of 5 °C/min. During charging (heating), an endothermic melting peak at 43.6 °C indicates latent heat absorption, while during discharging (cooling), a pronounced exothermic peak at 39 °C confirms effective latent heat release. Fig. 3(b) shows TGA profile of lauric acid that indicates retaining 96.2% mass up to 205 °C, followed by a sharp single-step degradation between 205 and 280 °C, resulting in 95.9% total weight loss and only 0.3% residual mass, confirming high thermal purity and stability for thermal energy storage applications. Additionally, Table 2 summarizes the thermophysical properties of Lauric acid which was estimated (melting point and latent heat) and obtained from supplier document.

3.2. Climatic condition variation

Fig. 4 shows the diurnal variation of solar irradiance and ambient temperature from 9:00 to 22:00 h. Solar irradiance increases from 09:00 h, reaches a peak value of 986 W/m^2 between 13:00–14:00 h, and then decreases, with a sharper decline after 16:00 h due to reduced solar zenith angle. The average irradiance during sunshine hours is approximately 715 W/m^2. Ambient temperature rises from 31 °C at 9:00 h to a maximum value of 41.1 °C slightly after 14:00 h, reflecting effect of thermal inertia that causes lag in ambient temperature as shown in Fig. 4.

3.3. Heat storage duration and heat discharge behavior

Heat storage duration and discharge behavior have been evaluated on the basis of the thermal evolution of lauric acid temperature; in fact, the time span during which the PCM remains at or above the melting point (43.6 °C) has been used to directly evaluate the persistence of the phase transition and the efficiency of the latent heat retention under real operational conditions. In CSS-PCM, PCM temperature marginally touches the melting point only between 13:00–15:00 h, peaking maximum PCM temperature in the range of 38–42 °C by thermocouples placed at different locations, leads to a short residence time (soon after 17:00 h) and predominantly sensible heat storage and partial latent heat storage. In HSSS-PCM, PCM temperature reached 40–44 °C at 14:00 h and remained above 43.6 °C from 13:00 to 16:30–17:00 h, that leads to extend the storage duration (till 19:00 h) but still indicating partial latent heat utilization. In contrast, HSSS-PCM-ME exhibited an earlier onset of melting (12:00 h), a higher peak temperature reached 42–48 °C at 14:00 h, and sustained PCM temperature above 43.6 °C until 17:00–17:30 h. This extended storage duration (up to 22:00 h) confirms complete phase transition and superior latent heat utilization efficiency. Table 3 summarizes the fraction of stored thermal energy released during the discharging period. It was estimated from the experimentally observed PCM temperature decay and the duration for which the PCM remained above its melting temperature, following established practice in PCM-based latent thermal energy storage studies [44–46].

3.4. Heat storage efficiency of lauric acid

From an advanced thermodynamic perspective, storage capacity represents only the theoretical potential of a PCM to store heat. In

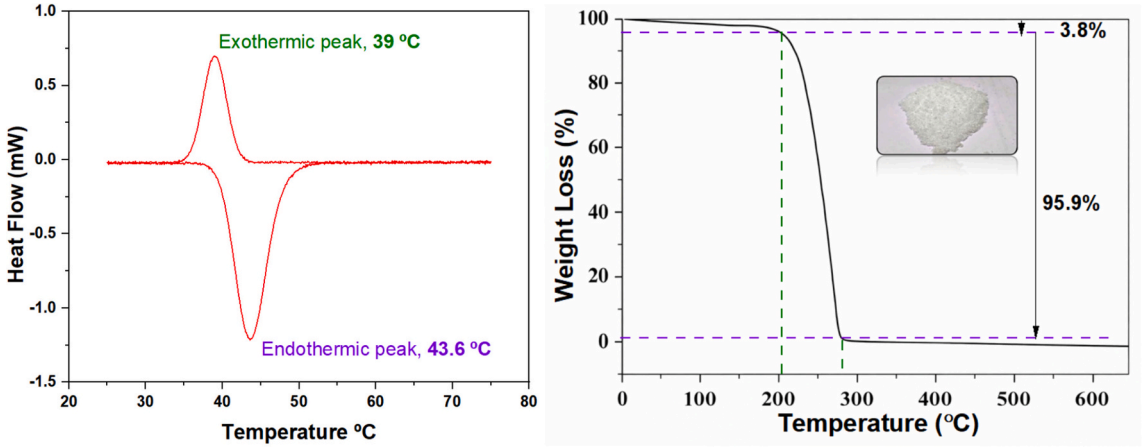

Fig. 3. Characterization results of Lauric acid (a) DSC heating and cooling curve with melting point (onset), and (b) TGA analysis.

Table 2
Summary of thermophysical properties of lauric acid [45].

S.N.	Thermophysical property	Value
1.	Latent heat of fusion (L_f)	181–183 kJ/kg
2.	Melting point	43.6 °C
3.	Specific heat Cp (solid: 25 °C)	2.1 kJ/kg°C
4	Specific heat Cp (liquid: 44 °C)	3 kJ/kg°C
5.	Thermal conductivity	0.16 W/m°C
6.	Density (solid)	1007 kg/m^3
7.	Density (liquid)	862 kg/m^3

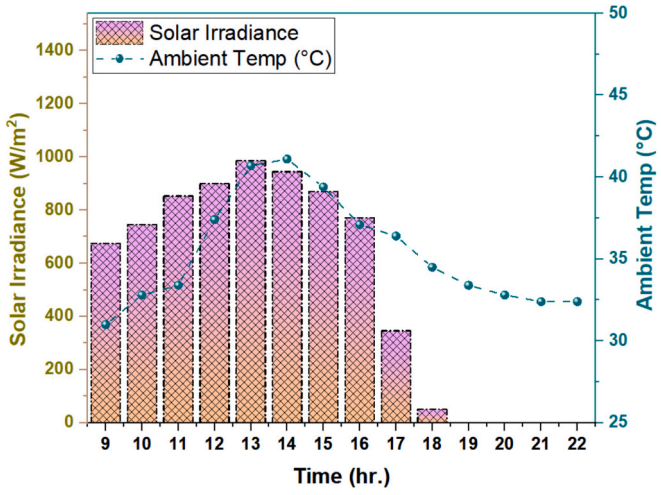

Fig. 4. Diurnal variation of solar irradiance and ambient temperature with time on a clear-sky day

contrast, storage efficiency quantifies the actual fraction of that heat effectively recovered under real discharge kinetics. It inherently accounts for heat transfer resistance, phase-change completeness, and discharge dynamics. Consequently, storage efficiency provides a more realistic measure of functional performance. In the CSS-PCM system, a steep post-17:00 h discharging slope causes PCM temperature to fall below 43.6 °C shortly after sunset, resulting in negligible storage duration and a low efficiency of 31.9%. The HSSS-PCM configuration exhibits a reduced discharging rate, maintaining PCM temperature above the melting point until 18:30–19:00 h and achieving a moderate efficiency of 51.5%. In contrast, the U-tube macro-encapsulated PCM displays the lowest discharging rate and sustains PCM temperature above 43.6 °C until 22:00 h, yielding an effective storage duration of nearly 5 h and a high efficiency (79.5%) as summarizes in Table 3 with formulations. To calculate heat storage efficiency, sensible heat stored (SHS) and useful heat released were calculated at instantaneous temperatures of PCM (T_{PCM}) and basin water (T_w) taking reference of initial condition of PCM ($T_{(PCM,initial)}$) and basin water. Further, a ± 10% sensitivity analysis was performed to confirm the results varied under permissible limit.

3.5. Sensitivity analysis of heat storage efficiency

A sensitivity analysis was conducted over latent heat storage efficiency by varying the fraction of useful heat release (f) by ±10% to account for uncertainty in temperature-based discharge estimation as shown in Eq. (7). A ± 10% sensitivity range is selected because it represents a realistic and balanced uncertainty band for temperature-based energy estimation without becoming trivial or excessively extreme. This kind of study is common in energy storage-based engineering applications [46]. The resulting efficiencies showed absolute deviation of ±3.2%, ±5.1%, ±7.9% from actual storage efficiencies as estimated and summarized in Table 4. The results indicate low sensitivity, consistent

Table 3
Heat storage efficiency calculation based on fraction of heat released of PCM.

Parameter	Formulation	CSS-PCM	HSSS-PCM	HSSS-PCM-ME
PCM mass (kg)	–	15	15	15
Latent heat stored (LHS) (kJ)	mL_f	2715	2715	2715
Sensible heat stored (SHS) (kJ)	$\sum (m_{PCM} c_{p,PCM} \times (T_{PCM,} - T_{PCM,initial}))$	333	423	558
Total heat stored (THS) (kJ)	$LHS + SHS$	3048	3138	3273
Useful heat released (UHR) (kJ)	$\sum (m_{PCM} \times c_{p,PCM} \times (T_{PCM} - T_w))$	972	1615	2601
Fraction of heat released (f)	$f = \frac{Q_{UHR}}{Q_{THS}}$	0.319	0.515	0.795
Heat storage efficiency (%)	$\frac{Q_{UHR}}{Q_{THS}} \times 100$	**31.9**	**51.5**	**79.5**

behavior and perseverance of performance hierarchy.

$$f_{low} = 0.9f, \quad f_{high} = 1.1f, \eta_{storage} = f \times 100 \tag{15}$$

3.6. Role of U-tube macro-encapsulation in enhancing storage efficiency

The enhanced total heat storage and heat storage efficiency of the U-tube macro-encapsulated PCM are achieved due to its line contact with the FRP absorber surface, which restricts heat loss from the absorber surface. In the U-tube configuration, the circumferential exposure and integrated absorber surface are exposed to the basin water temperature, which creates a low thermal resistance in heat transfer without significant loss to the ambient, in contrast to the other two configurations. CSS-PCM and HSSS-PCM exhibit lower peak PCM temperatures and shorter phase-change durations (less 2 h), and lower storage efficiencies (31.9–51.5%). In contrast, direct copper-water contact enables higher PCM temperature (56 °C), sustained melting until 22:00 h (around 5 h storage), and 79.5% efficiency. Fig. 5 illustrates a radar plot of results comparing PCM-based latent thermal energy storage configurations with respect to normalized charging kinetics, peak PCM temperature, phase-change duration, discharging behavior, and absolute storage efficiency. All values are normalized (0–1) so trends, not magnitudes, are compared, which is best practice to illustrate multiparameter results. The U-tube macro-encapsulated PCM system demonstrates consistently superior storage performance across all metrics.

3.7. Basin water and condenser surface temperature variation

Fig. 6(a) shows the variation of basin water and condenser surface temperature for the CSS-PCM, HSSS-PCM, and HSSS-PCM-ME configurations, in direct response to the solar irradiance and ambient temperature trends presented in Fig. 4. During daytime, when solar irradiance increases from about 675 to 986 W/m^2 and ambient temperature rises from 31 to 41.5 °C, basin water temperatures increase gradually. The condenser surface temperatures remain lower than the basin water temperatures, provides favorable condition for vapor transport and condensation under relatively low thermal gradients. At peak solar conditions (13:00–14:00 h), when irradiance reached 986 W/m^2, the basin water temperature reaches maximum values of 56 °C for HSSS-PCM-ME, 53 °C for HSSS-PCM, and 51 °C for CSS-PCM. The higher basin water temperatures observed in the HSSS-PCM-ME can be directly attributed to its hemispherical geometry, which enables enhanced interception of solar radiation throughout the day and reduces reflective losses compared to the planar glass covers of CSS-PCM and HSSS-PCM. Simultaneously, the condenser surface temperatures rise to about 43 °C (HSSS-PCM-ME), 46 °C (HSSS-PCM), and 42 °C (CSS-PCM). After 15:00 h, solar irradiance declines sharply from approximately 870 W/m^2 to 346 W/m^2 by 17:00 h, along with a reduction in ambient temperature being observed. As a result, both basin water and condenser temperatures decrease in response to ambient condition. At 17:00 h, basin water temperatures drop to around 44 °C (HSSS-PCM-ME), 35 °C (HSSS-PCM), and 33 °C (CSS-PCM), indicating reduced evaporation potential. During overnight hours (19:00–22:00 h), when solar irradiance is zero, basin water temperatures stabilize between 25 and 35 °C, closely following ambient conditions. Average basin water temperature after sunset was 30.0 °C, 30.66 °C, 36.66 °C with CSS-PCM, HSSS-PCM, and HSSS-PCM-ME respectively.

Table 4
Summary of sensitivity analysis over storage efficiency by ±10% varying the fraction of released thermal energy (f).

Configuration	At 10% less thermal energy release		Actual thermal energy release		At 10% high thermal energy release	
	$f_{-10\%}$	$\eta_{-10\%}$ (%)	f_{actual}	η_{actual} (%)	$f_{+10\%}$	$\eta_{+10\%}$ (%)
CSS-PCM	0.287	28.7	**0.319**	**31.9**	0.351	35.1
HSSS-PCM	0.464	46.4	**0.515**	**51.5**	0.567	56.7
HSSS-PCM-ME	0.716	71.6	**0.795**	**79.5**	0.875	87.5

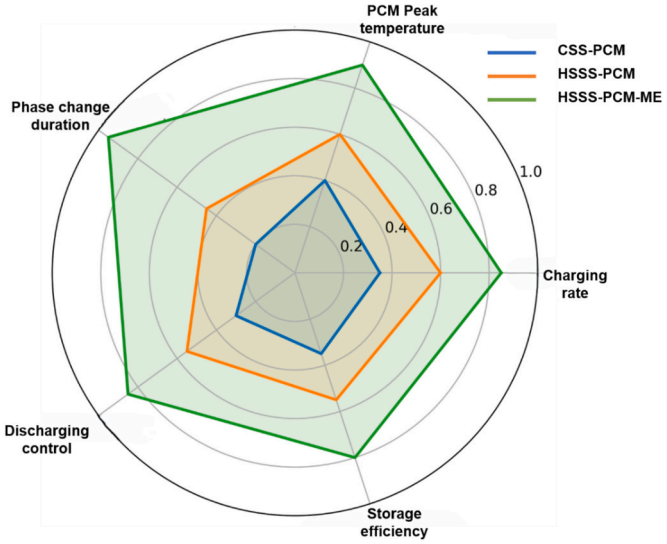

Fig. 5. Radar chart comparing normalized latent heat storage performance of CSS-PCM, HSSS-PCM, and HSSS-PCM-ME based on charging rate, peak PCM temperature, phase-change duration, discharging control, and storage efficiency.

3.8. Temporal behavior and temperature gap between PCM and basin water

Fig. 6(b)–(d) presents the temporal behavior of lauric acid and favorable temperature gap between PCM and basin water to transfer the stored latent heat from PCM to basin water.

3.8.1. CSS-PCM configuration

During the daytime, the basin water and the average PCM temperature increased linearly with solar irradiation. By around 13:00 to 14:00 h., the basin water temperature reaches its highest point of 51 °C, whereas the PCM temperature continues to rise throughout the charging period. It was found that, after sunsets, the basin water temperature falls faster than the PCM temperature. After 16:00 h, the positive temperature differential illustrated by the red bars in Fig. 6(b) indicates that the PCM temperature is greater than the basin water temperature, creating a favorable thermal difference that transfers latent heat to the basin water through the absorber surface. However, because of the lower peak water temperature and insufficient storage of heat, the effect was minimal.

3.8.2. HSSS-PCM configuration

In this configuration, the basin water temperature was generally higher than that for CSS-PCM. During peak sunshine, the basin water temperature reached 53 °C for the HSSS-PCM, and this increase directly correlated with increased solar exposure due to the system's hemispherical condenser configuration, as evidenced by higher condenser and basin temperatures compared to CSS-PCM. The PCM temperature follows the basin water temperature during the charging cycle, however, during the overnight duration, the PCM temperature is significantly higher than the basin water temperature as shown in Fig. 6(c), indicating that the system effectively stored energy and released it as needed. Although the temperature difference between the PCM and the water during the cooling period is larger than that observed in CSS-PCM, the PCM maintains a relatively constant temperature until at least 19:00 h. This prolonged thermal duration allows for continuous evaporation

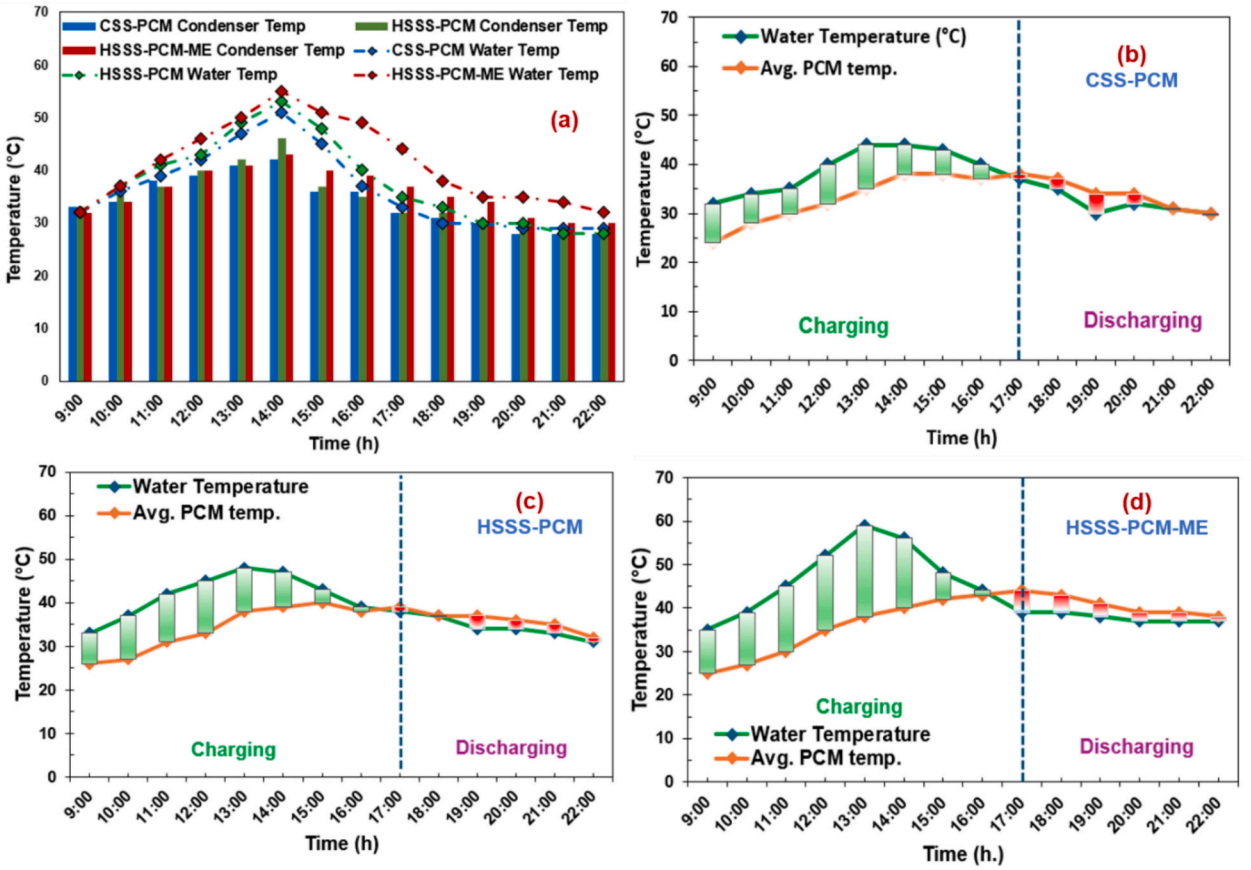

Fig. 6. (a) Daytime variation of condenser surface (glass) and basin saline water temperature for CSS-PCM, HSSS-PCM, and HSSS-PCM-ME solar still configurations. (b–d) Temporal variation of the temperature difference between basin saline water and average PCM temperature for (b) CSS-PCM, (c) HSSS-PCM, and (d) HSSS-PCM-ME systems.

post the peak sun hours.

3.8.3. *HSSS-PCM-ME configuration*

The most significant thermal enhancement is observed in the HSSS configuration. During peak irradiance hours (13:00–14:00 h), the basin water temperature rises to 56 °C, higher than both CSS-PCM and HSSS-PCM configurations. This behavior is consistent with earlier observations, where the hemispherical geometry demonstrated superior solar energy interception and reduced optical losses. The PCM in HSSS-PCM-ME attains higher charging temperatures and exhibits a larger favorable temperature difference between PCM and basin water after sunset as shown in Fig. 6(d). From 17:00 h onward, the PCM temperature remains consistently higher than basin water temperature, resulting in sustained heat release during overnight time. Consequently, basin water temperatures remain above 38–40 °C until 22:00 h, extending the effective evaporation period.

3.9. *Charging and discharging rate of PCM*

Charging and discharging rate of PCM is asymmetric in basin water heating. Charging rate should be high to ensure efficient thermal energy storage and reduce heat loss to surrounding. Fig. 6(b), (c), and (d) gives the insights of charging and discharging rate. Charging rate was estimated during the sunshine period from 9 to 17 h. During this period maximum charging rate was 2.38 °C/h for HSS-PCM-ME, while HSSS-PCM and CSS-PCM showed 1.63 and 1.75 °C/h respectively. Indicating superior heat transfer and efficient thermal storage behavior of novel U-tube encapsulation geometry with HSSS. Whereas, during 5 h. of period from 17 h to 22 h, rate of discharging was moderate and controlled in HSSS-PCM-ME of −1.2 °C/h whereas HSSS-PCM and CSS-PCM shows −1.4 and − 1.6 °C/h. Summary of slope-based analysis of PCM temperature rise and fall is tabulated in Table 5.

3.10. *Hourly and cumulative yield*

Hourly freshwater cumulative yield (9:00 to 22:00 h) trend of three systems is compared and shown in Fig. 7. During daytime (9:00 to 17:00 h) freshwater yield increased steadily from 9:00 to 14:00 h for all systems, following the rise in solar irradiance. Maximum hourly yields at 14:00 h were approximately 310 mL/m^2 for CSS-PCM, 345 mL/m^2 for HSSS-PCM, and 385 mL/m^2 for HSSS-PCM-ME. After 15:00 h, yield from CSS-PCM and HSSS-PCM declined rapidly, whereas HSSS-PCM-ME sustained higher production due to better heat retention and utilization. At 17:00 h, HSSS-PCM-ME produced 270 mL/m^2, compared to 185 mL/m^2 (CSS-PCM) and 225 mL/m^2 (HSSS-PCM). After this, latent heat storge comes into play because at the peak hour basin water temperature crossed (CSS-PCM-51 °C, HSSS-PCM- 53 °C and HSSS-PCM-ME- 55 °C) the melting point of lauric acid.

After sunset, it can be observed that overnight yield (17:00–22:00 h) was decreasing in all three systems. At 20:00 h, HSSS-PCM-ME produces

Table 5
Summary of slope-based analysis of PCM temperature to estimate the charging and discharging rate (negative sign indicate discharging).

System	Charging rate (°C/h)	Discharging rate (°C/h)
CSS-PCM	1.75	−1.60
HSSS-PCM	1.63	−1.40
HSSS-PCM-ME	2.38	−1.20

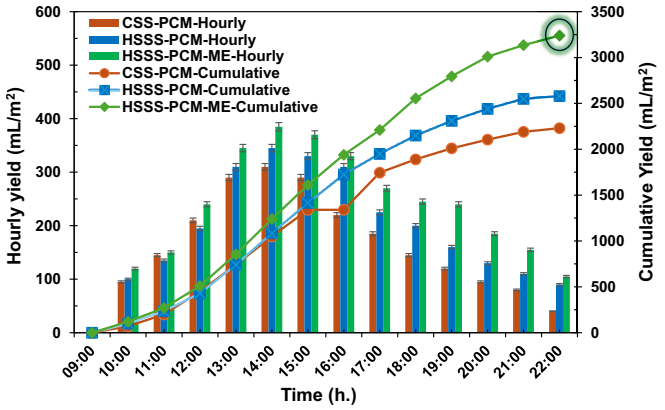

Fig. 7. Hourly and cumulative yield from CSS-PCM, HSSS-PCM and HSSS-PCM-ME

185 mL/m^2, while CSS-PCM dropped below 100 mL/m^2. This resulted in overnight freshwater collection of 1030 mL/m^2 for the HSSS-PCM-ME, whereas the HSSS-PCM and CSS-PCM collects 590 mL/m^2 and 605 mL/m^2, respectively, clearly illustrating the effect of more efficient PCM discharge to extend the production time of the still. CSS-PCM and HSSS-PCM were almost on same level of yield that shows its low capability of storing heat and utilizing less efficiently. Based on cumulative yield slope, it is noticed that HSSS-PCM-ME yield at higher rate with steeper slope compared to other two systems as shown in Fig. 7. Eventually, cumulative yield at 22:00 h reached 2350 mL/m^2 with CSS-PCM, 2580 mL/m^2 with HSSS-PCM, and 3240 mL/m^2 with HSSS-PCM-ME.

3.11. Thermal and exergy efficiency of solar stills

Fig. 8 compares the freshwater yield, thermal efficiency, and exergy efficiency of the CSS-PCM, HSSS-PCM, and HSSS-PCM-ME. The observed performance trends are a direct consequence of the enhanced basin water temperatures, prolonged heat retention due to encapsulation strategy, and reduction in heat loss to ambient. The freshwater daytime yield increases progressively from CSS-PCM of 2350 mL/m^2 to HSSS-PCM of 2580 mL/m^2 and reaches a maximum value of 3240 mL/m^2 with HSSS-PCM-ME. Compared to CSS-PCM, the HSSS-PCM showed a yield improvement of about 10%, while the HSSS-PCM-ME exhibits a substantial enhancement of nearly 37.87%. In comparison to HSSS-PCM, the HSSS-PCM-ME has a greater yield of 25.58%. A high yield in HSSS-PCM-ME can be due to the higher temperatures of basin water that facilitates longer evaporation caused by unique encapsulation layout compared to heat transfer from bottom of surface.

Similar trends were observed in terms of thermal efficiency. Thermal efficiency for CSS-PCM was 31.5%. for HSSS-PCM was 34.75%. Both systems were outperformed by HSSS-PCM-ME with thermal efficiency of 44.22% on daily basis in a similar moderate sunshine condition. Analysis highlights that there was a 10.3% increment in thermal efficiency for HSSS-PCM over CSS-PCM, and a 40.3% enhancement in HSSS-PCM-ME over CSS-PCM. It can be concluded that these improvements are due to better use of solar irradiation for evaporation and condensation with HSSS-PCM-ME, which correlates well with the higher and prolonged basin water temperatures observed in the HSSS-PCM-ME design.

Exergy efficiencies showed a larger relative improvement than thermal efficiencies. Exergy efficiencies of 2.47% for CSS-PCM and 2.81% for HSSS-PCM were obtained, while the exergy efficiency for HSSS-PCM-ME was 3.4%. Hence, the exergy efficiency of HSSS-PCM was 13% higher than that of CSS-PCM, and the exergy efficiency of HSSS-PCM-ME was 37.65% higher than that of CSS-PCM. The higher exergy efficiency of HSSS-PCM-ME indicates reduced irreversibility and improved thermodynamic quality of energy conversion compared to the other two systems. Moreover, it reveals that SSs are fundamentally low-temperature systems that generate high entropy. The focus here is not on generating work, but on achieving a phase change to convert the saline water into freshwater. Consequently, despite an efficient thermal process, the process remains inefficient in terms of exergy. The propagated error in the thermal efficiency was ±2.05% and exergy efficiency was ±4.1%, were estimated using Table 1 and Eqs. (7)–(9).

3.12. Comparative study with published work

Table 6 provides a systematic comparison between the present study

Table 6
Comparison of present work with previous published work.

Work	Thermal efficiency	Exergy efficiency
Present work (HSS-PCM-ME)	**44.40%**	**3.2%**
Hemispherical shape-Abdelgaied et al. [47]	45.45%	2.7%
Encapsulation-Vigneswaran et al. [48]	37%	3.2%

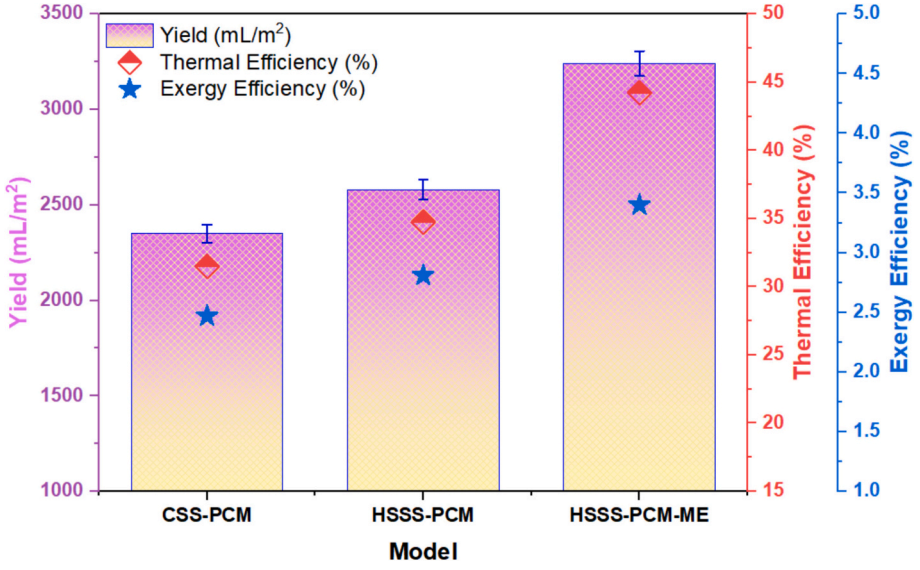

Fig. 8. Solar still performance comparison at cumulative yield, thermal efficiency and exergy efficiency parameters

and previously reported works on hemispherical solar stills integrated with PCM and encapsulation techniques, highlighting the relative improvements in productivity, thermal efficiency, and exergy performance achieved in this work.

3.13. Freshwater quality testing

Freshwater quality (yield water) test is crucial for determining device effectiveness. In experimental investigation, simulated saline water of total dissolved solid (TDS) was 35,000 ppm used as a feed water in basin of all three solar stills. Distilled water obtained from HSSS-PCM-ME was taken as after treatment sample. Parameters such as TDS, pH, electrical conductivity (EC) and dissolved oxygen are crucial parameters to judge the water quality hence sample testing before and after treatment was carried out at Central Instrumentation Facility (CIF). Further, quality is compared with WHO standards to ensure safety. Complete quality test is summarized into Table 7.

3.14. Energy-economic-enviro analysis

The energy-economic analysis confirms that the HSSS-PCM-ME system delivers superior performance despite its higher fabrication cost (₹16,000). It achieves the highest freshwater cumulative yield of 3.24 L/day and annual production of 972 L/year, which is 38% higher than CSS-PCM. This leads to the maximum annual gain of ₹19,440/year, while maintaining a comparable payback period of 10.3 months as summarized in Table 8 (row 1–7). Additionally, it utilizes the highest solar energy (610.2 kWh/year), indicating more effective energy conversion and utilization. Overall, the HSSS-PCM-ME offers the best economic return due to its higher productivity and efficient solar energy use.

Based on environmental assessment, the HSSS-PCM-ME system shows the greatest CO_2 reduction potential, avoiding 565.65 kg/year (CEA) and 207.8 kg/year (IPCC), which is 25–38% higher than other systems as summarized in Table 8 (row 8–10). This is directly linked to its higher solar energy utilization, reducing dependence on conventional energy sources. Thus, it demonstrates the most sustainable performance with maximum emission mitigation and energy efficiency.

4. Conclusions

From present experimental investigation, it can be assured that the thermal behavior of the phase change material (PCM) is controlled by maximum temperature, phase-change duration, and controlled discharging, which all impact the percentage of the stored energy that can be used efficiently. Lauric acid, demonstrated differences in energy usage among the three configurations. Maximum basin water temperature, with CSS-PCM reached 51 °C, with HSSS-PCM reached 53 °C and HSSS-PCM-ME reached 56 °C. Based on total heat stored and heat released highlight, a short phase-change duration (less than 2 h) and low energy usage fractions of 0.319 and 0.515, corresponded to a storage efficiency of 31.9% and 51.5%, respectively. The U-tube macro-encapsulated configuration stayed at or above its melting temperature until 22:00 h and achieved a significantly greater fraction of the energy stored as useful energy of 0.795, providing the greatest storage efficiency of 79.5%. Sensitivity analysis conducted with a ± 10% variation in the released-energy fraction, showed absolute deviation in efficiency of ±3.2%, ±5.1%, ±7.9% with CSS-PCM, HSSS-PCM, and HSSS-PCM-ME, respectively from actual storage efficiencies indicating low sensitivity, consistent behavior and perseverance of performance hierarchy. The improvement in thermal storage capability also directly enhanced the performance of the solar still system. The yield of freshwater produced per day was enhanced from 2350 mL/m^2 with CSS-PCM to 2580 mL/m^2 with HSSS-PCM and then to 3240 mL/m^2 with HSSS-PCM-ME. Similar to the freshwater production in overnight (17:00–22:00 h), the water yields for each configuration were 605 mL/m^2, 590 mL/m^2, and 1030 mL/m^2, respectively, demonstrating the value of sustained latent heat. Additionally, the thermal and exergy efficiencies of the system increased from 34.61% and 2.47% with CSS-PCM to 38.74% and 2.81% with HSSS-PCM and 44.22% and 3.4% with HSSS-PCM-ME. Water quality testing ensures the condensed yield qualify the water WHO guidelines. A techno-economic assessment of the all three systems demonstrated that despite the higher fabrication cost of the HSSS-PCM-ME (₹16,000), it had a shorter payback time of 10.3 months. An environmental assessment of the CSS-PCM-ME systems demonstrated a maximum CO_2 mitigation potential of 565.65 kg/year for the HSSS-PCM-ME.

Table 7
Water quality testing before and after the treatment.

S. N.	Parameters	Before treatment	After treatment	WHO standards
1.	TDS (ppm)	35,000	68	<300
2.	pH	6.5	7.5	6.5–8.5
3.	EC (μS/cm)	21,755	33.4	0–800
4.	Dissolved oxygen (mg/L)	5.1	7.1	6.5–8

Table 8
Comparative techno-economic-enviro analysis of CSS-PCM, HSSS-PCM, and HSSS-PCM-ME system [41].

S.N.	Performance indicator	Formulation	CSS-PCM	HSSS-PCM	HSSS-PCM-ME
1	Total fabrication cost (TFC), Rs.	Total material + Fabrication cost	11,500	13,500	16,000
2	Annual first cost (AFC), Rs./year	TFC × MRF (0.277)	3185.5	3739.5	4432
3	Annual maintenance cost (AMC), Rs./year	20% of AFC	637.1	747.9	884.4
4	Daily freshwater yield, L/day	–	2.35	2.58	3.24
5	Average annual production (AAP), L/year	Avg. daily yield × 300 days	705	774	972
6	Overall annual gain (OAG), Rs./year	AAP × S.P.	14,100	15,480	19,440
7	**Payback period (PP), months**	**TFC / (OAG − AMC)**	**10.2**	**10.9**	**10.3**
8	Utilized solar energy (E_{solar}), kWh/year	AAP × L_{fg}/3600	442.75	485.9	610.2
9	**CO_2 avoided (CEA baseline), kg/year**	**0.927 (CEA India baseline)**	**410.41**	**450.42**	**565.65**
10	CO_2 avoided (IPCC baseline), kg/year	0.340 (IPCC)	150.5	165.5	207.8

CRediT authorship contribution statement

Vikash Kumar Chauhan: Writing – original draft, Formal analysis, Data curation, Conceptualization. **Pushkar Singh:** Visualization, Validation. **Rohit Kumar Singh:** Formal analysis, Data curation. **Suresh Pratap:** Formal analysis, Data curation. **Vineet Singh:** Software, Methodology. **Shailendra Kumar Shukla:** Writing – review & editing,

Resources, Project administration.

Declaration of Generative AI and AI-assisted technologies in the writing process

No generative AI tools are used in the generation of data, analysis, interpretation of results, or writing of the manuscript. All scientific content was investigated, reviewed, and validated entirely by the authors.

Funding

Authors declare that no funds, grants, or other support were received for this work from any public or private body.

Declaration of competing interest

The authors have no relevant financial and non-financial interests to disclose.

Acknowledgment

Authors would like to express sincere gratitude to affiliated organizations for their lab facilities especially Mechanical Engineering Department and Workshop, G. L. Bajaj Institute of Technology and Management, Gr. Noida and CERD lab, Mechanical Engineering department, IIT BHU for providing lab testing and recording facility with required space to conduct the experiments.

Data availability

Data will be made available on request.

References

[1] V. Mishra, K. Thirumalai, S. Jain, S. Aadhar, Unprecedented drought in South India and recent water scarcity, Environ. Res. Lett. 16 (2021) 054007, https://doi.org/10.1088/1748-9326/abf289.
[2] G. Baggio, M. Qadir, V. Smakhtin, Freshwater availability status across countries for human and ecosystem needs, Sci. Total Environ. 792 (2021) 148230, https://doi.org/10.1016/j.scitotenv.2021.148230.
[3] Progress on level of water stress – 2024 update, UN-Water, 2024. https://www.unwater.org/publications/progress-level-water-stress-2024-update.
[4] A.K. Thakur, R. Sathyamurthy, R. Saidur, R. Velraj, I. Lynch, N. Aslfattahi, Exploring the potential of MXene-based advanced solar-absorber in improving the performance and efficiency of a solar-desalination unit for brackish water purification, Desalination 526 (2022) 115521, https://doi.org/10.1016/j.desal.2021.115521.
[5] S. Kiran, S. Singh, C. Keske, G. Diaz, Feasibility of desalination by solar stills for small community scale freshwater demand, J. Clean. Prod. 379 (2022) 134595, https://doi.org/10.1016/j.jclepro.2022.134595.
[6] S.K. Hota, S.S. Hada, C. Keske, G. Diaz, Feasibility of desalination by solar stills for small community scale freshwater demand, J. Clean. Prod. 379 (2022) 134595, https://doi.org/10.1016/J.JCLEPRO.2022.134595.
[7] L.D. Jathar, S. Ganesan, K. Shahapurkar, M.E.M. Soudagar, M.A. Mujtaba, A. E. Anqi, M. Farooq, A. Khidmatgar, M. Goodarzi, M.R. Safaei, Effect of various factors and diverse approaches to enhance the performance of solar stills: A comprehensive review, J. Therm. Anal. Calorim. 147 (7) (2021) 4491–4522, https://doi.org/10.1007/S10973-021-10826-Y.
[8] A. Pugsley, A. Zacharopoulos, J.D. Mondol, M. Smyth, Global applicability of solar desalination, Renew. Energy 88 (2016) 200–219, https://doi.org/10.1016/j.renene.2015.11.017.
[9] M. Jahanpanah, S.J. Sadatinejad, A. Kasaeian, M.H. Jahangir, H. Sarrafha, Experimental investigation of the effects of low-temperature phase change material on single-slope solar still, Desalination 499 (2021) 114799, https://doi.org/10.1016/J.DESAL.2020.114799.
[10] M. Saad.Mustafa, M.G. Mousa, M.M.K. Dawood, T.M. Mansour, T. Nabil, Energy, exergy, economic and environmental analysis of single slope solar still system using phase change material, Results Eng. 24 (2024) 103108, https://doi.org/10.1016/J.RINENG.2024.103108.
[11] R. Agrawal, K.D.P. Singh, Experimental investigation and computational modelling of double slope solar still integrated with eutectic phase change material, J. Energy Storage 52 (2022) 104802, https://doi.org/10.1016/J.EST.2022.104802.
[12] A.E. Kabeel, R. Sathyamurthy, A.M. Manokar, S.W. Sharshir, F.A. Essa, A. H. Elshiekh, Experimental study on tubular solar still using graphene oxide nano particles in phase change material (NPCM's) for fresh water production, J. Energy Storage 28 (2020) 101204, https://doi.org/10.1016/J.EST.2020.101204.
[13] M. Elashmawy, M. Alhadri, M.M.Z. Ahmed, Enhancing tubular solar still performance using novel PCM-tubes, Desalination 500 (2021) 114880, https://doi.org/10.1016/J.DESAL.2020.114880.
[14] N. Mekki, O. Ghriss, A. Bouabidi, K.A. Hammoodi, S.A. Kadhim, 4 E analysis of pyramid solar still with heat storage using different PCM layer thickness: energy, exergy, economic, and enviro-economic, J. Energy Storage 130 (2025) 117374, https://doi.org/10.1016/J.EST.2025.117374.
[15] M.E.A.E. Ahmed, S. Abdo, M.A. Abdelrahman, O.A. Gaheen, Finned-encapsulated PCM pyramid solar still – experimental study with economic analysis, J. Energy Storage 73 (2023) 108908, https://doi.org/10.1016/J.EST.2023.108908.
[16] A. Ibrahim, A. El-Sebaii, S. Aboul-Enein, M. Hegazy, A. Fleafl, A. EL-Monem Khallaf, Thermal performance enhancement of the wick-type solar still using titanium dioxide nanoparticles embedded in paraffin wax as a phase change material, Environ. Sci. Pollut. Res. 30 (49) (2022) 106812–106821, https://doi.org/10.1007/S11356-022-24374-X.
[17] H.R. Goshayeshi, I. Chaer, M. Yebiyo, H.F. Öztop, Experimental investigation on semicircular, triangular and rectangular shaped absorber of solar still with nano-based PCM, J. Therm. Anal. Calorim. 147 (4) (2021) 3427–3439, https://doi.org/10.1007/S10973-021-10728-Z.
[18] H. Ajdari, A. Ameri, Performance assessment of an inclined stepped solar still integrated with PCM and CuO/GO nanocomposite as a nanofluid, J. Build. Eng. 49 (2022) 104090, https://doi.org/10.1016/J.JOBE.2022.104090.
[19] S. Kumar, O. Prakash, S. Kumar, O. Prakash, Improving the single-slope solar still performance using solar air heater with phase change materials, Energies 15 (15) (2022), https://doi.org/10.3390/EN15218013.
[20] M. Dashtban, F.F. Tabrizi, Thermal analysis of a weir-type cascade solar still integrated with PCM storage, Desalination 279 (2011) 415–422, https://doi.org/10.1016/J.DESAL.2011.06.044.
[21] A.E. Kabeel, Y.A.F. El-Samadony, W.M. El-Maghlany, Comparative study on the solar still performance utilizing different PCM, Desalination 432 (2018) 89–96, https://doi.org/10.1016/J.DESAL.2018.01.016.
[22] A. Mosaffa, Shortcomings of PCMs in LHTS, 2025, pp. 31–49, https://doi.org/10.1007/978-981-95-3742-6_3.
[23] M. Faegh, M.B. Shafii, Experimental investigation of a solar still equipped with an external heat storage system using phase change materials and heat pipes, Desalination 409 (2017) 128–135, https://doi.org/10.1016/J.DESAL.2017.01.023.
[24] M.M. Thalib, A.M. Manokar, F.A. Essa, N. Vasimalai, R. Sathyamurthy, F.P. G. Marquez, M.M. Thalib, A.M. Manokar, F.A. Essa, N. Vasimalai, R. Sathyamurthy, F.P.G. Marquez, Comparative study of tubular solar stills with phase change material and nano-enhanced phase change material, Energies 13 (13) (2020), https://doi.org/10.3390/EN13153989.
[25] Z.H. Hasan, A.M. Hadi, W.A. Abd Al-wahid, D.M. Hachim, Numerical investigation of hemispherical solar still performance with optimal amount of PCM as a heat storage, Heat Transfer 54 (2025) 3031–3039, https://doi.org/10.1002/HTJ.23335. ;JOURNAL:JOURNAL:15206556;WGROUP:STRING:PUBLICATION.
[26] M. El Hadi Attia, M.E. Zayed, A.E. Kabeel, A.S. Abdullah, M. Abdelgaied, Energy, exergy, and economic analyses of a modified hemispherical solar distiller augmented with convex absorber basin, wicks, and PCM, Sol. Energy 261 (2023) 43–54, https://doi.org/10.1016/J.SOLENER.2023.05.057.
[27] U.F. Alqsair, A.S. Abdullah, M.M. Younes, Z.M. Omara, F.A. Essa, Augmenting hemispherical solar still performance: A multifaceted approach with reflectors, external condenser, advanced wick materials, and nano-PCM integration, Case Stud. Therm. Eng. 61 (2024) 104890, https://doi.org/10.1016/J.CSITE.2024.104890.
[28] P.B. Salunkhe, P.S. Shembekar, A review on effect of phase change material encapsulation on the thermal performance of a system, Renew. Sust. Energ. Rev. 16 (2012) 5603–5616, https://doi.org/10.1016/J.RSER.2012.05.037.
[29] D. Singh, D. Buddhi, A. Karthick, Productivity enhancement of solar still through heat transfer enhancement techniques in latent heat storage system: a review, Environ. Sci. Pollut. Res. 30 (1) (2022) 44–77, https://doi.org/10.1007/S11356-022-23964-Z.
[30] T. Sathish, R. Saravanan, J. Giri, A.O. Hourani, N. Becheikh, B.B. Bettaieb, A. J. Santhosh, A. Anderson, Advanced thermal optimization of solar stills using encapsulated phase change materials and graphene oxide nanoparticles for enhanced energy efficiency, Eng. Rep. 7 (2025) e70186, https://doi.org/10.1002/ENG2.70186;WGROUP:STRING:PUBLICATION.
[31] J.R. Patel, U. Shrivastava, Y. Naresh, J. Banerjee, Enhancing pyramidal solar still performance with a cost-effective PCM encapsulation technique: a heat transfer and 6E analysis study, Renew. Energy 253 (2025) 123630, https://doi.org/10.1016/J.RENENE.2025.123630.
[32] M. Abdelgaied, M.E.H. Attia, A.E. Kabeel, M.E. Zayed, Improving the thermo-economic performance of hemispherical solar distiller using copper oxide nanofluids and phase change materials: experimental and theoretical investigation, Sol. Energy Mater. Sol. Cells 238 (2022) 111596, https://doi.org/10.1016/J.SOLMAT.2022.111596.
[33] F.A. Essa, W.H. Alawee, A.S. Abdullah, S.A. Mohammed, A. Basem, H.S. Majdi, Z. M. Omara, Enhancing water evaporation rate in hemispherical solar distillers through innovative modifications and Nano-PCM integration, Sol. Energy 271 (2024) 112453, https://doi.org/10.1016/J.SOLENER.2024.112453.
[34] M.R. Rahi, S. Ostadi, A. Rahmani, M. Dibaj, M. Akrami, Studying the improvement of solar collector mechanism with phase change materials, Energies 17 (2024) 1432, https://doi.org/10.3390/EN17061432.

[35] S. Ataya, M.M. Elsayad, M. Ismail, S.W. Sharshir, 9E/3S assessment of a novel hybrid heat storage material incorporated inside a hemispherical distiller with an external condenser, Sep. Purif. Technol. 384 (2026) 136252, https://doi.org/10.1016/J.SEPPUR.2025.136252.
[36] B. Thamarai Kannan, B. Madhu, A.E. Kabeel, A.K. Thakur, R. Velraj, I. Lynch, R. Saidur, R. Sathyamurthy, Improved freshwater generation via hemispherical solar desalination unit using paraffin wax as phase change material encapsulated in waste aluminium cans, Desalination 538 (2022) 115907, https://doi.org/10.1016/J.DESAL.2022.115907.
[37] M. Saad.Mustafa, M.G. Mousa, M.M.K. Dawood, T.M. Mansour, T. Nabil, Energy, exergy, economic and environmental analysis of single slope solar still system using phase change material, Results Eng. 24 (2024) 103108, https://doi.org/10.1016/J.RINENG.2024.103108.
[38] R. Sathyamurthy, Experimental analysis of solar still equipped with porous rubber sheet as energy storage material, Sci. Rep. 15 (1) (2025) 8156, https://doi.org/10.1038/s41598-025-93148-5.
[39] R. Petela, Exergy of undiluted thermal radiation, Sol. Energy 74 (2003) 469–488, https://doi.org/10.1016/S0038-092X(03)00226-3.
[40] A.H. Mohammed, M. Attalla, A.N. Shmroukh, Comparative study on the performance of solar still equipped with local clay as an energy storage material, Environ. Sci. Pollut. Res. 29 (49) (2022) 74998–75012, https://doi.org/10.1007/S11356-022-21095-Z.
[41] S.K. Suraparaju, A. Sampathkumar, S.K. Natarajan, Experimental and economic analysis of energy storage-based single-slope solar still with hollow-finned absorber basin, Heat Transfer 50 (2021) 5516–5537, https://doi.org/10.1002/HTJ.22136;JOURNAL:JOURNAL:15206556;ISSUE:ISSUE:DOI.
[42] M.O. Khalaf, M.R. Özdemir, H.S. Sultan, A comprehensive review of solar still technologies and cost: Innovations in materials, design, and techniques for enhanced water desalination efficiency, Water 17 (2025) 1515, https://doi.org/10.3390/W17101515.
[43] C. Cao, Sustainability and life assessment of high strength natural fibre composites in construction, in: Advanced High Strength Natural Fibre Composites in Construction, 2017, pp. 529–544, https://doi.org/10.1016/B978-0-08-100411-1.00021-2.
[44] S. Shoeibi, N. Rahbar, A. Abedini Esfahlani, H. Kargarsharifabad, A comprehensive review of Enviro-Exergo-economic analysis of solar stills, Renew. Sust. Energ. Rev. 149 (2021) 111404, https://doi.org/10.1016/J.RSER.2021.111404.
[45] O. Khan, M. Parvez, P. Kumari, Z. Yahya, A. Alhodaib, A.K. Yadav, A.K. Shukla, Optimization of thermal performance in lauric acid-based phase change materials using a priority clustering approach, Energy Storage 6 (2024) e70026, https://doi.org/10.1002/EST2.70026;CTYPE:STRING:JOURNAL.
[46] X. Ma, Q. Zhang, J. Wang, C. Yue, Sensitivity analysis and optimization of structural parameters of a phase change material based multi-tube heat exchanger under charging condition, J. Energy Storage 56 (2022) 105940, https://doi.org/10.1016/J.EST.2022.105940.
[47] M. Abdelgaied, M.E.H. Attia, A.E. Kabeel, M.E. Zayed, Improving the thermo-economic performance of hemispherical solar distiller using copper oxide nanofluids and phase change materials: experimental and theoretical investigation, Sol. Energy Mater. Sol. Cells 238 (2022) 111596, https://doi.org/10.1016/J.SOLMAT.2022.111596.
[48] V.S. Vigneswaran, G. Kumaresan, B.V. Dinakar, K.K. Kamal, R. Velraj, Augmenting the productivity of solar still using multiple PCMs as heat energy storage, J. Energy Storage 26 (2019) 101019, https://doi.org/10.1016/J.EST.2019.101019.